Acta Astronautica 208 (2023) 281–295

Contents lists available at ScienceDirect

Acta Astronautica

journal homepage: www.elsevier.com/locate/actaastro

Combustion dynamics of high Mach number scramjet under different inflow thermal nonequilibrium conditions

Yu Ao [a,b], Kun Wu [a,*], Hongbo Lu [c], Feng Ji [c], Xuejun Fan [a,b]

[a] State Key Laboratory of High Temperature Gas Dynamics, Institute of Mechanics, Chinese Academy of Sciences, Beijing, 100190, China
[b] School of Engineering Sciences, University of Chinese Academy of Sciences, Beijing, 100049, China
[c] China Academy of Aerospace Aerodynamics, 100074, Beijing, China

ARTICLE INFO

Keywords:
Hypervelocity combustion
Thermal nonequilibrium
Two-temperature model
Numerical simulation

ABSTRACT

To characterize the impact of thermal nonequilibrium conditions in shock-induced combustion in high Mach number scramjet engines, a comparative numerical investigation has been performed. The combustor configuration was based on the HyShot II scramjet while the total enthalpy is 3.3 MJ/kg which resembles Mach 8 flight condition. The improved delay detached eddy simulation with Park two-temperature approach in combination with the vibration-chemical coupling model was employed in the nonequilibrium simulations. It is shown that under thermal nonequilibrium inflow conditions, noticeable stratification in the thermal state exists in the circumferential direction both in the combustor section and exhaust nozzle. In the inner core where the fuel mixes with the mainstream, flow deceleration caused by the heat release leads to a sufficient transformation of energy between the vibrational and translational-rotational modes approaching the thermal equilibrium state. However, the $\tau_{v,mix}$ is quite large in the supersonic mainstream, whereby the thermal nonequilibrium dominates. For the case with higher T_v in the inflow, the fuel jet's penetration height is lower while the local viscosity is higher which results in poor mixing between the fuel and air stream. Nevertheless, a 400 K increase in inflow T_v gives a higher effective temperature, which promotes the dissociation reactions, shortens the ignition distance and yields an 8% increase in the overall combustion efficiency. With better combustion performance, an additional 6% deceleration in the supersonic mainstream and the energy exchange rate between vibrational and translational-rotational modes becomes almost four times faster at the combustor outlet, which promotes the restoration of the thermal equilibrium state. Furthermore, under higher inflow vibrational temperature, the shock-induced combustion in supersonic crossflow becomes less stable with noticeable fluctuations in combustion heat release and local static pressure.

1. Introduction

Scramjet engine is one of the most recent innovations in the field of hypersonic technologies, which is of great significance for space exploration, military and transportation [1]. However, with the increase in the flight Mach number, scramjet engines will encounter a series of challenges. Firstly, the extremely short residence time makes it difficult for mixing between the fuel and mainstream to achieve reliable ignition and stable combustion. More importantly, as the flight Mach number increases, the stagnation temperature of the mainstream increases significantly, which will excite the vibrational mode of the molecules and even make the molecules start to dissociate and ionize [2]. The redistribution of molecular internal energy requires a large number of molecular collisions, and the energy of each mode regains Boltzmann distribution after a certain relaxation time. Due to the short relaxation time required, the rotational and translational modes are considered to be in equilibrium generally. The vibrational mode requires molecular collisions of several orders of magnitude higher to reach equilibrium with the translational mode. Thermal nonequilibrium in this work refers to the condition that the vibrational temperature is not equal to the translational temperature in the flow field. The ratio of the flow characteristic timescale to the vibrational relaxation timescale, i.e., the thermal Damköhler number Ω, is commonly used to characterize the thermal state of the gas [3], which is defined as $\Omega = \tau_{residence}/\tau_{vib}$. The flow can be considered to be in thermal equilibrium when $\Omega \gg 1$. The flow is the thermal frozen flow for $\Omega \ll 1$. When $\Omega \approx 1$, the flow is in

---

* Corresponding author.
E-mail address: wukun@imech.ac.cn (K. Wu).

https://doi.org/10.1016/j.actaastro.2023.04.020
Received 7 November 2022; Received in revised form 18 February 2023; Accepted 11 April 2023

thermal nonequilibrium state.

In the field of thermal nonequilibrium flows, researches on re-entry vehicles [4–6] and hypersonic cones [7,8] are more common, while few research efforts have been reported on nonequilibrium affected supersonic combustion for scramjet engines. Under thermal nonequilibrium conditions, considerable disparities were found regarding the locations and strength of the shock wave system in the isolator of the scramjet engines, which consequently alters the inflow conditions of the combustor. For instance, Han et al. [9] conducted a study on the effect of thermal nonequilibrium in a scramjet without fuel injection. It was found that the thermal nonequilibrium effect caused the intersection of the oblique shocks generated from the ramp to move downstream. Fiévet et al. [10] observed that, in the isolator, the edge of the shock structure was closer to the upstream and the pseudoshock structure was more compact due to thermal nonequilibrium effect. In addition, Gehre et al. [3] found that the temperature distribution of the first hot pocket changed significantly because of thermal nonequilibrium, which affects the subsequent chemical reactions.

Chemical reactions are more likely to occur in states that possess larger internal energies, so vibrational energy would play an important role in the reactions [11]. For example, molecules at high vibrational states are more likely to undergo dissociation reactions [12]. Further, thermal nonequilibrium effects have a great impact on the processes of mixing, ignition and combustion in high Mach number scramjet engines. For instance, Fiévet et al. [13] performed separate thermal equilibrium/nonequilibrium combustion simulations for a scramjet engine, where thermal nonequilibrium effect significantly accelerated the ignition by changing the local mixing as well as the dissociation reaction rates. Nevertheless, this finding was inconsistent with the observation in H_2 jet lift flame at high Mach number, where Koo et al. [14] suggested that thermal nonequilibrium effect would lead to longer flame lift distances and stronger combustion intensity in jet flames. Recently, Yao et al. [15] investigated a hydrogen-fueled scramjet engine at Mach number 10 and confirmed that the thermal nonequilibrium effect would inhibit the fuel propagation upstream and change the flame stabilization position. Therefore, the impacts of thermal nonequilibrium effect on the performance of scramjet engines at hypervelocity and high enthalpy conditions still need to be understood more comprehensively and accurately, which is closely related to the design and optimization of Mach number scramjet engines.

To investigate the combustion characteristics of scramjets at high Mach numbers, flight tests and ground-based high enthalpy shock tunnel tests are widely used at present. Unfortunately, the flow structures and combustion instability of the scramjet engines could differ significantly at varying altitude conditions, and an increase in flight altitude leads to a decrease in combustion efficiency [16]. In actual flight tests, changes in flight altitude, speed and posture will change the flow field in the inlet ramp, resulting in an unstable extent of thermal nonequilibrium at the combustor inlet. On the other hand, in the ground-based experiments, the thermal nonequilibrium effect in the high enthalpy shock tunnel is significant [17], and it can directly affect the performance prediction of scramjet engines. Besides, the extent of thermal nonequilibrium effect at the combustor inlet are not the same for different operating conditions, and it may affect our interpretation of the experiment results. Therefore, understanding the effect of the thermal nonequilibrium conditions on the combustion dynamics is indispensable for accurate prediction of engine performance of high Mach number scramjets.

With this background, we aimed to employ the improved delay detached eddy simulation (IDDES) [18] to investigate the effect of different inflow thermal nonequilibrium conditions on the combustion dynamics of the HyShot II scramjet corresponding to the 28 km-altitude flight condition [19]. The previous study of Fiévet [20] reported the fact that ignoring thermal nonequilibrium effect in the Hyshot II scramjet will overestimate the ignition delay time and underestimate the combustion intensity. Taking the same engine operating condition as a baseline, the effect of inflow thermal nonequilibrium condition on the combustion dynamics of the Hyshot II scramjet will be thoroughly discussed in this work.

The organization of the remainder of the paper is as follows. We describe the physical models and numerical methods first, then the computational configuration and numerical details are presented. After numerical validation, the mixing and combustion characteristics under thermal nonequilibrium condition are illustrated. It is then followed by a detailed discussion on the influence of the inflow thermal nonequilibrium extent on the combustion dynamics. At last, the main concluding remarks are given in Section 5.

2. Physical models and numerical methods

2.1. Governing equations and the two-temperature model

The unsteady and three-dimensional Favre-filtered compressible reactive Navier-Stokes governing equations are given by

$$\frac{\partial \overline{\rho}}{\partial t}+\frac{\partial \overline{\rho}\widetilde{u}_j}{\partial x_j}=0 \tag{1}$$

$$\frac{\partial \overline{\rho}\widetilde{u}_j}{\partial t}+\frac{\partial \overline{\rho}\widetilde{u}_i\widetilde{u}_j}{\partial x_j}=-\frac{\partial \overline{p}}{\partial x_i}+\frac{\partial \overline{\tau}_{ij}}{\partial x_j}+\frac{\partial \tau_{ij}}{\partial x_j} \tag{2}$$

$$\frac{\partial \overline{\rho}\widetilde{Y}_k}{\partial t}+\frac{\partial \overline{\rho}\widetilde{u}_j\widetilde{Y}_k}{\partial x_j}=\frac{\partial}{\partial x_j}\left(\overline{\rho}D_k\frac{\partial \widetilde{Y}_k}{\partial x_j}\right)-\frac{\partial \gamma_{k,j}}{\partial x_j}+\overline{\omega}_k,\ k=1,\dots,N_S \tag{3}$$

in which “ – ” and “~” represent spatial and Favre-filtered quantities, respectively. And $\overline{\rho}$ is the density of the mixture, $\overline{p}$ is the static pressure recovered from the partial pressures using Dalton’s law. Furthermore, $\widetilde{u}_j$ $(j=1,2,3)$ is the velocity components. $\overline{\tau}_{ij}$ is the viscous stress tensor, and τ_{ij} is the turbulent stress tensor. $\widetilde{Y}_k$ denotes the mass fraction of the k^{th} one among the N_S species, $\gamma_{k,j}$ is the turbulent species diffusion term, and D_k is mixture-averaged mass diffusivity of species k, which is obtained by using the modified Wilke’s law. $\overline{\omega}_k$ is the filtered mass production of species k.

As the characteristic temperatures related to the electronic mode of energy are usually very high. The electronic excitation can be ignored for low to moderate Mach number flows, and it is only necessary to include electronic excitation for flows with extremely high Mach number $\mathrm{Ma}\geq 15$ [21]. Thus, for most engineering applications as concerned in the present work, expressing internal energy in terms of translational, rotational and vibrational modes is sufficient. Because the rotational energy relaxation is very fast compared to vibrational energy relaxation, the translational and rotational modes of energy are assumed to be in thermal equilibrium, and can be represented by a single translational-rotational temperature T_{tr}. Furthermore, under the assumption that vibrational-vibrational (V–V) relaxation occurs very quickly, the vibrational energy mode can be characterized by the vibrational temperature T_v. This is the rationale of Park’s two-temperature model [12], which was employed to model the thermal nonequilibrium flow in the present simulation. Correspondingly, the vibrational energy of species k at vibrational temperature T_v is given by

$$e_{vk}=R_k\frac{\theta_{vk}}{exp\left(\frac{\theta_{vk}}{T_v}\right)-1} \tag{4}$$

in which θ_{vk} represents the characteristic vibrational temperature of the k^{th} species as listed in Table 1, R_k stands for the species gas constant. The

Table 1
The characteristic vibrational temperature of the species [22].

	N_2	O_2	H_2	H_2O	OH
θ_v [K]	3371	2274	6332	2295/5262/5404	5378

vibrational energy of the mixture can be obtained by

$$e_v = \sum_{k=1}^{N_S} Y_k e_{vk} \tag{5}$$

The total specific energy e of the mixture consists of the specific internal and kinetic energies

$$e_{tot} = \sum_{k=1}^{N_S} Y_k e_k + \frac{1}{2}u^2 \tag{6}$$

where e_k is the specific internal energy of species k, given by the sum of the contribution of translational energy e_{tk}, rotational energy e_{rk}, vibrational energy e_{vk} and the energy of formation e_{0k}:

$$e_k = e_{tk}(T_{tr}) + e_{rk}(T_{tr}) + e_{vk}(T_v) + e_{0k} \tag{7}$$

in which the translational-rotational and vibrational energies are calculated as

$$e_{tk}(T_{tr}) + e_{rk}(T_{tr}) = C_{v,tr}^k T_{tr} = (3/2R_k + R_k)T_{tr} \tag{8}$$

$$e_{vk}(T_v) = C_{v,v}^k T_v = R_k \left(\frac{\theta_{vk}}{T_v}\right)^2 \frac{\exp\left(\frac{\theta_{vk}}{T_v}\right)}{\left(exp\left(\frac{\theta_{vk}}{T_v}\right) - 1\right)^2} T_v \tag{9}$$

Subsequently, the filtered transport equation of the total energy and vibrational energy can be expressed as

$$\frac{\partial \overline{\rho}\widetilde{e}_{tot}}{\partial t} + \frac{\partial \widetilde{u}_j\left(\overline{\rho}\widetilde{e}_{tot} + \overline{p}\right)}{\partial x_j} = \frac{\partial}{\partial x_j}\left(\lambda_{tr}\frac{\partial \widetilde{T}_{tr}}{\partial x_j} + \lambda_v \frac{\partial \widetilde{T}_v}{\partial x_j} - \gamma_{T,j} + \sum_{k=1}^{N_S} \overline{\rho} D_k \widetilde{h}_k \frac{\partial \widetilde{Y}_k}{\partial x_j}\right) + \frac{\partial}{\partial x_j}\widetilde{u}_i\left(\overline{\tau}_{ij} + \tau_{ij}\right) \tag{10}$$

$$\frac{\partial \overline{\rho}\widetilde{e}_v}{\partial t} + \frac{\partial \overline{\rho}\widetilde{u}_j\widetilde{e}_v}{\partial x_j} = \frac{\partial}{\partial x_j}\left(\lambda_v \frac{\partial \widetilde{T}_v}{\partial x_j}\right) + \mathcal{Q}_{T-V} + \mathcal{Q}_{C-V} \tag{11}$$

in which $\widetilde{h}_k = \widetilde{e}_k + \overline{p}/\overline{\rho}$ is the specific enthalpy. ν is the molecular viscosity, and υ_t is the turbulent viscosity. The pressure value is obtained via $\overline{p} = \sum_{k=1}^{Ns} \overline{\rho}\widetilde{Y}_k R_u \widetilde{T}_{tr}/M_k$ with R_u and M_k being the universal gas constant and molecular weight of species k. The transport properties of the gas mixture are calculated using Gupta's mixing rule [2] with the collision integrals data provided by Wright et al. [23]. Moreover, the λ_v is thermal conductivity of vibrational energy, which is calculated by the CEA empirical formula $\lambda_v = \mathrm{A}\ \ln T_v + \frac{\mathrm{B}}{T_v} + \frac{\mathrm{C}}{T_v^2} + D$ while the model coefficients can be found in Ref. [24].

The source term $\mathcal{Q}_{T-V}$ represents the energy exchange between translational-rotational and the vibrational modes, while $\mathcal{Q}_{C-V}$ denotes the vibrational energy added or removed by chemical reactions, which will be detailed in the following. γ_{Tj} is the turbulent energy flux term. Here, the viscous stress tensor $\overline{\tau}_{ij}$ is given by

$$\overline{\tau}_{ij} = \overline{\rho}\nu\left(\frac{\partial \widetilde{u}_i}{\partial x_j} + \frac{\partial \widetilde{u}_j}{\partial x_i} - \frac{2}{3}\delta_{ij}\frac{\partial \widetilde{u}_k}{\partial x_k}\right) \tag{12}$$

The turbulent stress tensor τ_{ij} can be expressed by

$$\tau_{ij} = \overline{\rho}\nu_t\left(\frac{\partial \widetilde{u}_i}{\partial x_j} + \frac{\partial \widetilde{u}_j}{\partial x_i} - \frac{2}{3}\delta_{ij}\frac{\partial \widetilde{u}_k}{\partial x_k}\right) - \frac{2}{3}\delta_{ij}\overline{\rho}k_t \tag{13}$$

The turbulent species diffusion term γ_{kj} and turbulent energy flux term γ_{Tj} are modeled as

$$\gamma_{k,j} = -\overline{\rho}\frac{\upsilon_t}{Sc_t}\frac{\partial \widetilde{Y}_k}{\partial x_j} \tag{14}$$

$$\gamma_{T,j} = -\overline{\rho}\frac{\upsilon_t}{Pr_t}\frac{\partial \widetilde{h}}{\partial x_j} \tag{15}$$

where Pr_t and Sc_t are the turbulent Prandtl and Schmidt numbers, whose values are set to 0.9 and 0.7, respectively.

The turbulent viscosity υ_t is obtained using the Spalart-Allmaras (S-A) one equation turbulence model [25] within the improved delayed detached-eddy simulation (IDDES) framework [18]. In this formulation, the spatial-filtered or Reynolds-averaged equations are solved in a uniform framework by equivalently treating the turbulent viscosity in the RANS mode and the subgrid viscosity in the LES mode. The background RANS model in the IDDES approach is the S-A turbulence model. For IDDES simulation, the subgrid length scale depends on not only local cell size but also the distance to the nearest wall. A shielding function is used to avoid deteriorating the detection of the boundary layer edge by excessively low subgrid viscosity, so that the boundary layer is fully covered by the RANS model. The same hybrid LES/RANS modeling approach has achieved desired successes in previous simulations for supersonic combustion [26] and hypersonic combustion with thermal nonequilibrium effect [15].

Regarding the energy relaxation source terms in Eq. (11), the Landau–Teller model [27] was employed in the present study, wherein the $\mathcal{Q}_{T-V}$ source term is modeled as

$$\mathcal{Q}_{T-V} = \sum_{k=1}^{N} \rho_k \frac{e_{vk}(T_{tr}) - e_{vk}(T_v)}{\tau_{k,V-T}} \tag{16}$$

$$\tau_{k,V-T} = \frac{\sum_k X_k}{\sum_k X_s/\tau_{m-k,V-T}} \tag{17}$$

where $\tau_{k,V-T}$ is the vibrational relaxation timescale of each species. X_k is the species molar fraction and $\tau_{m-k,V-T}$ is the interspecies relaxation timescale given by the Millikan-White semi-empirical correlation [28] and the Park correction [29]

$$\tau_{m-k,V-T} = \frac{1}{p} exp\left[A_{m,k}\left(T_{tr}^{-\frac{1}{3}} - B_{m,k}\right) - 18.42\right] + \frac{1}{\overline{c}_m \sigma_{v,m} n_{m,k}},\ \text{with } p \text{ in atm} \tag{18}$$

in which $A_{m,k}$ and $B_{m,k}$ are the model coefficients. $\overline{c}_m$ denotes the average molecular speed, $\sigma_{v,m}$ is the limited collision cross section, and $n_{m,k}$ is the number density of the colliding pair (m, k). These model coefficients are summarized as follow.

$$A_{m,k} = 1.16 \times 10^{-3}\sqrt{M_{m,k}\theta_{v,k}^{4/3}}, \quad B_{m,k} = 0.015 M_{m,k}{}^{1/4} \tag{19}$$

$$\overline{c}_m = \sqrt{\frac{8R_m T_{tr}}{\pi}}, \quad \sigma_{v,m} = \sigma_m\left(\frac{50000}{T_{tr}}\right)^2 \tag{20}$$

where the reduced molecular weight $M_{m,k} = M_m M_k/(M_m + M_k)$, M_m is molecular weight of species m, and σ_m is taken as $3 \times 10^{-21} m^2$ in this work. After the vibrational energy is obtained by solving Eq. (11), the vibrational temperature can be obtained by Newton's iterative method until the relative error been two successive solutions is lower than 10^{-4}:.

$$T_{v,n+1} = T_{v,n} - \left[e_v\left(p_n, T_{v,n}\right) - e_{v,n}\right] / C_{v,v}\left(p_n, T_{v,n}\right) \tag{21}$$

where $e_{v,n}$ denotes the vibrational energy of mixture calculated by Eq. (11). $T_{v,n}$, $e_v(p_n, T_{v,n})$ and $C_{v,v}(p_n, T_{v,n})$ present the vibrational temperature, vibrational energy and heat capacity at constant volume for the vibrational energy mode calculated with thermal dynamic variables from the last iteration, respectively. The $C_{v,v}$ of mixture can be obtained by $C_{v,v} = \sum_{k=1}^{N_S} Y_k C_{v,v}^k$, wherein specific heat capacity at constant volume for the vibrational energy mode can be found in Eq. (9). Likewise, the translation-rotational temperature was calculated in the similar way.

2.2. Chemical reactions and chemistry-vibration coupling

The chemical reactions in this work are modeled through the finite rate chemistry approach, whereby the chemical source term $\dot{\omega}_k$ can be represented as

$$\dot{\omega}_k = M_k \sum_{r=1}^{N_R} \left(\nu''_{k,r} - \nu'_{k,r}\right) \left[k_{f,r} \prod_{j=1}^{N_s} \left(\frac{\rho_j}{M_j}\right)^{\nu'_{j,r}} - k_{b,r} \prod_{j=1}^{N_s} \left(\frac{\rho_j}{M_j}\right)^{\nu''_{j,r}} \right] \tag{22}$$

in which N_R represents the number of reactions, ν'_k and ν''_k are the forward and backward reaction stoichiometry coefficients, respectively. $k_{f,r}$ and $k_{b,r}$ are the forward and backward reaction rates. The reaction rate for each reaction follows the modified Arrhenius form

$$k_r = A \times T_c^{\beta}\, exp\left(-\frac{T_a}{T_c}\right) \tag{23}$$

where A is the pre-exponential factor, β is the temperature exponent, T_a is the activation temperature, and T_c is the rate-controlling temperature for chemical reactions, respectively. The chemical mechanism, which contains 7 species and 9 reactions was used to calculate the reaction rates [30], which is detailed in Table 2 and Table 3.

To accommodate the influence of vibrational relaxation on the chemical reactions, the Park's T-Tv model [12] was adopted in the simulation. Evidently, the concept of the Arrhenius equations is that two molecules will react when the mutual energy exceeds a certain energy barrier. Hence, it is natural to assume that the dissociation of molecular species is obtained more easily when the molecules are vibrationally excited. To be specific, in this model, Park assumes that the dissociation reactions can be described by a single rate-controlling temperature, which is an appropriate average of the local translational-rotational and vibrational temperatures.

For a dissociation reaction, the T_c is defined as the Park effective temperature

$$T_{eff} = T_{tr}^{\alpha} \times T_v^{1-\alpha} \tag{24}$$

with the exponent α set to 0.7, and the rate-controlling temperature for other reaction schemes can be found in Table 3. The vibrational energy added or removed by chemical reaction, $\mathcal{Q}_{C-V}$ in Eq. (11), is obtained by the preferential model.

$$\mathcal{Q}_{C-V} = \sum_{k=1}^{N} 0.3\dot{\omega}_k \mathfrak{D}_k \tag{25}$$

wherein $\mathfrak{D}_k$ [31] is the dissociation potential energy of species k whose specific values are summarized in Table 4. In the preferential model, molecules at the higher vibrational energy states are more likely to undergo dissociation.

Table 2
Reaction scheme with its corresponding controlling temperature.

No.	Reaction	Forward, $T_{c,f}$	Backward, $T_{c,b}$
1	$O_2+M=O+O+M$	T_{eff}	T_{tr}
2	$H_2+M=H+H+M$	T_{eff}	T_{tr}
3	$H_2O+M=OH+H+M$	T_{eff}	T_{tr}
4	$OH+M=O+H+M$	T_{eff}	T_{tr}
5	$O_2+H=OH+O$	T_{tr}	T_{tr}
6	$H_2+O=OH+H$	T_{tr}	T_{tr}
7	$H_2O+O=OH+OH$	T_{tr}	T_{tr}
8	$H_2O+H=OH+H_2$	T_{tr}	T_{tr}
9	$H_2+O_2=OH+OH$	T_{tr}	T_{tr}

Table 3
H_2/O_2 reaction mechanism (unit: cm-g-s-K) [30].

No.	Forward rate constant			Reverse rate constant		
	A	β	T_a	A	β	T_a
1	7.2×10^{18}	− 1.0	59340	4.0×10^{17}	− 1.0	0
2	5.5×10^{18}	− 1.0	51987	1.8×10^{18}	− 1.0	0
3	5.2×10^{21}	− 1.5	59386	4.4×10^{20}	− 1.5	0
4	8.5×10^{18}	− 1.0	50830	7.1×10^{18}	− 1.0	0
5	2.2×10^{14}	0.0	8455	1.5×10^{13}	0.0	0
6	7.5×10^{13}	0.0	5586	3.0×10^{13}	0.0	4429
7	5.8×10^{13}	0.0	9059	5.3×10^{12}	0.0	503
8	8.4×10^{13}	0.0	10116	2.0×10^{13}	0.0	2600
9	1.7×10^{13}	0.0	24232	5.7×10^{11}	0.0	14922

Table 4
The dissociation potential energy of the species [31].

Species	N_2	O_2	H_2	H_2O	OH
Dissociation potential [J /kg]	3.36×10^7	1.54×10^7	2.16×10^8	2.70×10^7	2.70×10^7

3. Computational configuration and numerical details

The simulation model configuration is based on the HyShot II model combustor, which is schematized in Fig. 1. The model scramjet engine consists of an inlet ramp, a combustor and an exhaust nozzle. The angle between the inlet ramp and the combustor is 18°, and the model scramjet was mounted at a 3.6° angle-of-attack. There is a bleed slot between the inlet ramp and combustor, which is used to bleed off the shock and boundary layer, which was treat as zero-gradient boundary condition in the simulation by following Zheng [32]. The rectangular combustor is 300 mm in length, 75 mm in width and 9.8 mm in height. Four fuel injectors with a diameter of 2 mm are equally spaced along the spanwise direction on the combustor bottom wall, located 58 mm downstream of the combustor leading edge. The far-field inflow condition mimics a 28 km-altitude flight at *Ma* 7.37, whose specific values are summarized in Table 5.

To reproduce the conditions of the model scramjet, a zonal approach was adopted following [13,33,34], in which simulations of different fidelities were performed in a nested manner for the individual parts of the engine test rig according to Fig. 1. The combustor inflow conditions were obtained based on a two-dimensional (2D) planar RANS simulation. The RANS simulation was conducted with the same S-A turbulence model [18,35] using a nonequilibrium 5-step reaction mechanism [2,36]. The previous study [19] on the HyShot II scramjet has fully verified the rationality of the 2D inflow condition, and the results suggested that 2D simulations were relatively accurate to predict the position and strength of the shock wave structures. Likewise, the same approach was adopted in the researches of Karl et al. [33,37], Chapuis et al. [34] and Chen et al. [38]. Considering that altering the inflow conditions in subsequent studies, the 2D model was adopted to generate the combustor inflow in this study to reduce the overall computational cost.

To investigate the influence of thermal nonequilibrium effect on the combustion dynamics, two computational cases with the same stagnation enthalpy, possessing different vibrational temperatures are considered. To achieve this, the combustor section of the 2D RANS simulation model was extend in the streamwise direction to ensure that

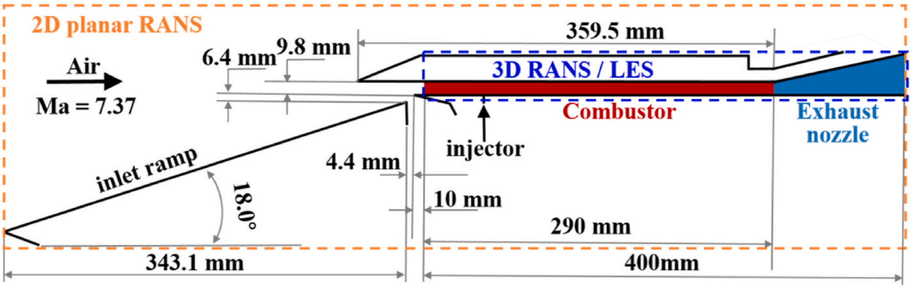

Fig. 1. Schematic of the model scramjet configuration [19].

Table 5
Air stream inflow conditions [19].

Property	Value	Unit
Static pressure, p_∞	1.988	kPa
Stagnation pressure, p_t	142	kPa
Static translational-rotational Temperature, $T_{tr,\infty}$	266	K
Static vibrational temperature, $T_{v,\infty}$	266	K
Mach number, Ma_∞	7.37	–
Stagnation enthalpy, h_0	3.30	MJ/kg
Velocity, U_∞	2414	m/s
Density, ρ_∞	0.0259	kg/m^3
Mass fraction, $Y_{N_2,\infty}$	0.77	–
Mass fraction, $Y_{O_2,\infty}$	0.23	–
Angle of attack, α	−3.6	°

the air flow has sufficient time for the energy exchange between different modes to occur. To ensure that the total enthalpy of the two cases is the same, the adiabatic, non-catalytic, slip condition is applied to the combustor wall. The average vibrational temperature at the $x = 0$ m cross-section is taken as a reference to find the downstream cross-section with an average vibrational temperature 400 K higher, and then those thermal-fluid variables at these two cross-sections are taken as the combustor inlet profiles. The T_v of case A and case B at the combustor inlet section are 688.38 and 1088.42 K respectively, and other operating conditions are given in Table 6 which are demonstrated in Fig. 2. The hydrogen fuel is injected with a stagnation temperature of 300 K, and the stagnation pressure is prescribed to match an overall equivalence ratio 0.295 for both cases.

With these combustor inflow profiles for both cases, the combustor section was simulated with the three-dimensional IDDES method subsequently. And to reduce the computational cost, one eighth of the combustor is considered, hence the computational domain spans 9.375 mm in the spanwise direction. As for the computational mesh grid, the block-structured hexahedral grid was generated for the computational domain for the 3D IDDES simulation, which is displayed in Fig. 3. In the wall-normal direction, the first layer cell size is 5 μm resulting in a non-dimensional cell height $y^+ \leq 1$. Grid refinements were imposed to the vicinity of the fuel injector and mixing layer between the fuel and the mainstream, as shown in Fig. 3 (b). The total number of grid cells was 8.2 million, while a coarser grid of 6.6 million and a finer grid of 11.5 million were used for the grid convergence study.

A density-based solver, HiSCFOAM-NonE (High speed combustion OpenFOAM solver with none equilibrium) was home-developed based on the OpenFOAM libraries. The central upwind interpolation scheme of Kurganov and Tadmor [39] was used for the convective fluxes, while the diffusive fluxes were discretized using central differencing scheme. The temporal integration was advanced by the second-order backward scheme. The parallel simulations were performed using 320 CPU cores on Tianhe-1 supercomputer in National Supercomputer Center of Tianjin. The integration was constrained by a maximum Courant-Friedrichs-Lewy number of 0.3, corresponding to an average time step of approximately 1.5 × 10^{-9} s. The averaged flow-through time is $\tau_f = 200$ μs, and the statistics were sampled over 4 τ_f after reaching the quasi-steady flow state.

Table 6
Averaged combustor inflow conditions.

Property	Case A	Case B	Unit
p_∞	127.23	119.37	kPa
$T_{tr,\infty}$	1512.33	1451.47	K
$T_{v,\infty}$	688.38	1088.42	K
U_∞	1786.07	1803.42	m/s
Equivalence Ratio, φ	0.295	0.295	–

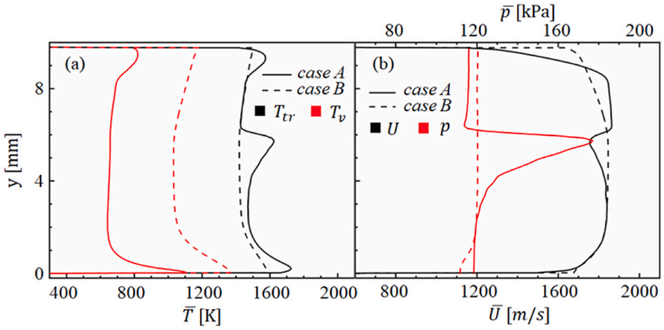

Fig. 2. Profiles of combustor entrance condition for the two cases with showing the (a) translational-rotational and vibrational temperatures and (b) the pressure and velocity, respectively.

4. Results and discussion

4.1. Experimental validation and grid convergence study

Since the fuel injection condition in the experiment is difficult to control accurately, three typical overall equivalence ratios [19] ranging from 0.266 to 0.351 are considered for the numerical validation. It can be observed from Fig. 4 that, in the numerical simulation, the pressure on the bottom wall undergoes slight fluctuations near the location where the fuel is injected. After that, the pressure distribution reveals a virtually linear increase along the combustor and reaches its maximum at the end of the combustion section, but also a precipitous decrease in wall pressure towards the end of the combustor. Good agreements between the experimental measurement and the simulation results are obtained, which confirms the reliability of the present simulation methodology.

For a grid independence study, state pressure along the combustor bottom wall predicted by three topologically similar grids consisting of 6.6 million, 8.2 million and 11.2 million cells are also displayed in Fig. 4. The pressure prediction by the medium mesh agrees favorably with that by the fine mesh, whereas the pressure predicted by the coarse mesh exhibits considerable variation due to premature boundary layer separation. Therefore, as a compromise between the computational cost and the numerical accuracy, the medium mesh was used for the following

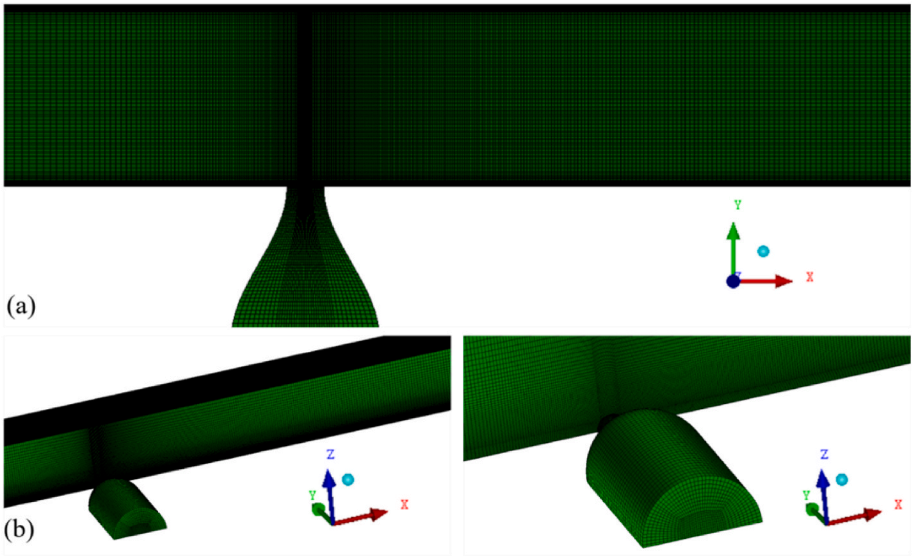

Fig. 3. The computational mesh (a) front view and (b) zoom-in view of the fuel injector.

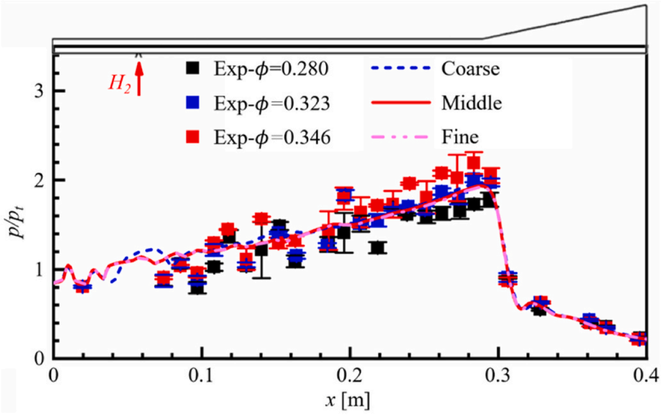

Fig. 4. Comparison of the experimental [19] and simulation results regarding the pressure measurement on the combustor bottom wall.

simulations.

4.2. Combustion characteristics under thermal nonequilibrium condition

In this section, the combustion characteristics under thermal nonequilibrium condition corresponding to case A will be illustrated. As can be seen from Fig. 5 (a), as the fuel jet enters the high speed crossflow, it deflects and turns along the main flow. Due to the difference in velocities, the fuel jet acts as an obstruction to the main supersonic crossflow and generates a bow shock ahead of the injector. In the meantime, the incoming supersonic turbulent boundary layer starts to separate ahead of the bow shock and a stable recirculation region is created upstream of the fuel injector. Subject to the huge velocity difference, the Kelvin-Helmholtz (K–H) instability emerges in the shear layer between the sonic fuel jet and the supersonic mainstream. The bow shock reflects from the combustor top wall and then the incidence shock wave impacts with the windward side of the jet shear layer, which stimulates the Richtmyer-Meshkov (R-M) instability and further accelerates the destabilization of the shear layer. In Fig. 5 (b), the supersonic mainstream decelerates obviously as it interacts and mixes with the fuel jet, whereas the overall flow Mach number is still larger than 1.2 with the downstream combustion heat release, which operates in the supersonic combustion mode. Finally, the flow undergoes rapid acceleration in the exhaust nozzle due to volumetric expansion.

It is clear in Fig. 6 (a) that the mass fraction of hydrogen in the transverse jet is still high within the first 10 jet diameters streamwise distance after the fuel is issued so that only a small amount of OH radicals and H_2O can be seen in the windward side of the shear layer. Further downstream, mixing between the fuel jet and the high speed mainstream under the action of both K–H and R-M instabilities, enhances the consumption of H_2. In Fig. 6 (b) and (c), ahead of the fuel injection location, small amounts of OH radicals and H_2O are produced in the recirculation region under high static temperature and relatively long residence time. Previous experiment [40] has also found that reactions occur in the recirculation region, and it plays an important role in the following flame stabilization. Since the final combustion product H_2O is mainly created by the chain carrying reaction $H_2 + OH = H_2O + H$, H_2O almost entirely resides in the shear layer and the area below the shear layer.

Fig. 7 (a) displays a superposition of the numerical schlieren and H radical's mass fraction contour. It is evident that after the impaction of the incidence shock waves, the mass fraction of H radical increases abruptly on the windward side of the fuel jet, demonstrating that high

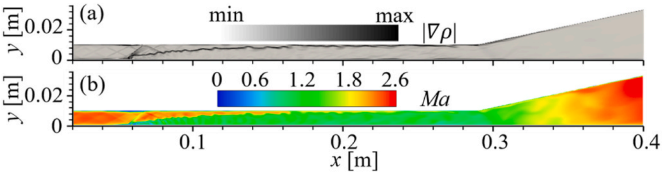

Fig. 5. Instantaneous contour of the (a) density gradient and (b) Mach number on the combustor central plane.

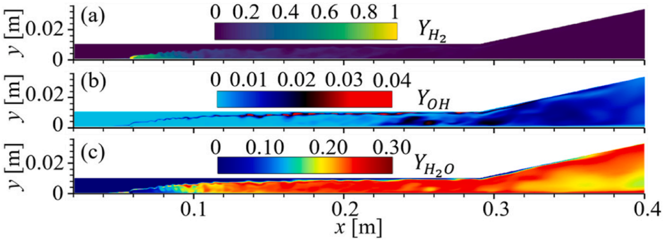

Fig. 6. Instantaneous contour of the (a) H_2 mass fraction, (b) OH mass fraction and (c) H_2O mass fraction on the combustor central plane.

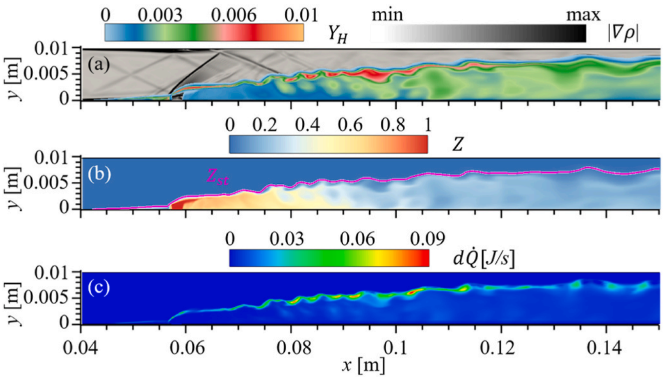

Fig. 7. Instantaneous contours of the (a) H mass fraction and density gradient, (b) mixture fraction and (c) heat release rate on the combustor central plane.

temperature and pressure induced by the shock waves accelerate the process of dissociation reactions [41]. The dissociation products such as H and O radicals, emerge in large quantities near the shear layer, diffuse toward the normal direction as the mixing enhancement and trigger other chain carrying reactions such as $H + O_2 = OH + O$. In Fig. 7 (b), with the mixing of the fuel and mainstream, the stoichiometric line of mixture fraction Z gradually moves toward the top wall and delineates the structure of the flame front. As shown in Fig. 7 (c), significant increase of $d\dot{Q}$ near the shear layer indicates that the combustion reactions occur mainly near the shear layer in the upstream of the combustor, which is in accordance with the flame front represented by the stoichiometric line in Fig. 7 (b).

In Fig. 8 (a), the variation of T_{tr} in the flow field behind the bow shock is drastic. T_{tr} of the mainstream is much higher than that of fuel jet, so the flow field shows a remarkable temperature stratification near the mixing shear layer. The reflected shock waves induce the formation of several hot spots near the shear layer [34], whereas the T_{tr} in the jet core remains low. With the assistance of the shock shear-layer interactions, T_{tr} approaches the auto-ignition temperature of hydrogen-air mixture at $x \approx 0.12$ m. Further downstream, the core flow of the fuel jet near the shear layer widens and forms twisted strips after flow destabilization. The diffusion flame keeps spreading towards the normal direction and approaching the top and bottom walls at $x \approx 0.22$ m. In this stage, the combustor transits to the fully developed turbulent combustion state, within which the fuel sufficiently reacts with air and the T_{tr} rises sharply.

Since the relaxation timescale of the vibrational energy mode is longer than that of the translational-rotational energy mode, the evolution of the vibrational temperature shows different characteristics. In Fig. 8 (b), the change of T_v after crossing the bow shock is relatively small. Comparing Fig. 8 (a) and (b), the difference between T_{tr} and T_v is noticeable before $x = 0.11$ m. Further downstream, the T_v rises gradually and approaches T_{tr} near the reacting shear layer, where the H_2 is fully mixed with the air stream. However, it is still in vibrational heating state near the top wall. There is almost no difference between the T_{tr} and T_v in the turbulent combustion region between streamwise locations $x =$ 0.16 and 0.30 m, wherein the thermal equilibrium state is established. In the simulation with thermal nonequilibrium, the effect of chemistry-vibration coupling is mainly manifested in the dissociation reactions, which is controlled by the effective temperature T_{eff}. In Fig. 8 (c), the T_{eff} is clearly lower than the T_{tr} in the region near the combustor inlet and the fuel injection location, so the thermal nonequilibrium caused by fuel mixing retards the process of the dissociation reactions there.

In Fig. 9 (a), the recirculation bubble generated by the adverse pressure is clearly observable upstream of fuel injection. The H_2 entrained into the recirculation bubble is not completely consumed due to the high local equivalence ratio. The perimeter of the fuel jet gradually becomes irregular under the cation of K–H and R-M instabilities. For jet in supersonic transverse cross flow, counter-rotating vortex pairs play an important role in the spreading of the flame [42] as shown in Fig. 9 (b)–(c). At downstream locations, the vortex structure continuously becomes larger and more distorted, which accelerates the mixing of fuel and air together with the K–H and R-M instabilities, thus enhancing the efficiency of combustion. In Fig. 9 (b), the combustion intermediate H radical diffuses outward radially while moving downstream. Although the flame gradually spreads outward, there is still a large amount of unreacted air flow around the fuel jet.

From plane A in Fig. 9 (b), it can be found that the high temperature caused by the hot spots near the shear layer accelerates the molecular collisions, which produces a large number of active radicals such as H and OH. In Fig. 9 (c), those active radicals participate in the subsequent chain reactions and release heat in the jet shear layer. The chemical

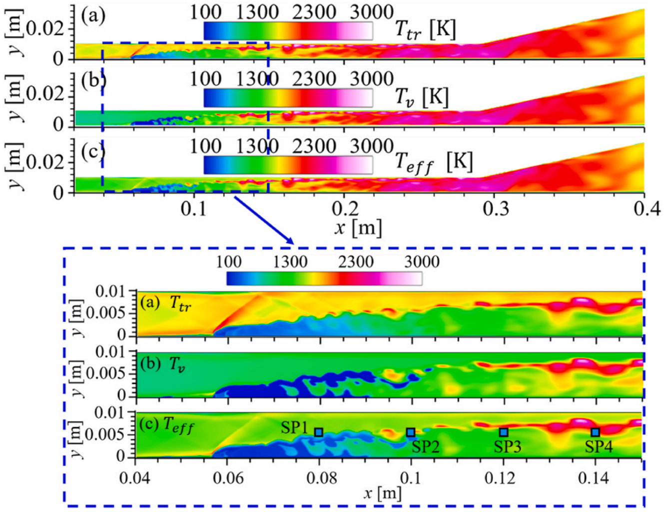

Fig. 8. Instantaneous contours of the (a) T_{tr}, (b) T_v and (c) T_{eff} on the combustor central plane. SP1, SP2, SP3 and SP4 denote sampling points at locations ($x = 0.08$, $y = 0.005$), ($x = 0.10$, $y = 0.005$), ($x = 0.12$, $y = 0.005$) and ($x = 0.14$, $y = 0.005$) on the combustor central plane, respectively (all units in m).

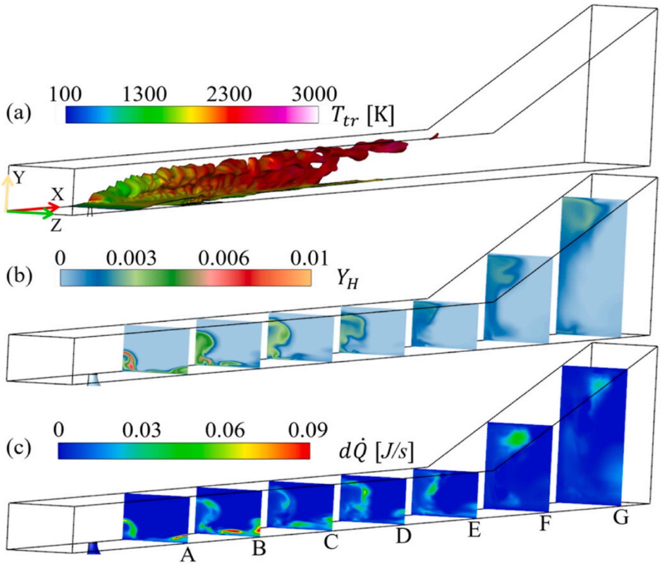

Fig. 9. (a) H_2 mass fraction iso-surface colored by the instantaneous translational-rotational temperature, instantaneous contour of (b) H mass fraction and (c) heat release rate at different streamwise locations. The cut planes A to G are located at the axial locations of $x = 80$, 130, 180, 230, 280, 330, and 380 mm, respectively.

reaction continues to release heat in the exhaust nozzle, while active radicals fail to recombine to form stable products due to insufficient residence time in the expansion section.

Temperature distributions at different streamwise locations are shown in Fig. 10. It can be seen from Fig. 10 (a), in plane A, the T_{tr} increases near the bottom wall, which can be attribute to those chemical reactions occurring in the low-speed wall boundary layer. From plane B to plane E, T_{tr} in the shear layer encompassing the fuel jet core rises significantly with the mixing between the fuel and high-speed mainstream. The T_{tr} decreases in the exhaust nozzle due to volumetric expansion, as the translational-rotational energy being transferred to the kinetic energy. On the contrary, in Fig. 10 (b), the T_v is quite lower than the T_{tr} near the fuel jet's shear layer in the plane A. Further downstream, T_{tr} and T_v in the inner core of the jet are almost identical, which indicates that the mixture in this region has achieved thermal equilibrium state. However, in the combustor section, the T_v of the supersonic mainstream out of the fuel jet periphery is lower than the T_{tr}, which is still in the vibrational heating state. While in the exhaust nozzle, the T_v in the supersonic mainstream is higher than the T_{tr}, which is in the vibrational cooling state.

Fig. 11 presents the spatial distribution of the vibrational relaxation timescale of the mixture $\tau_{v,mix} = 1/\sum_{k=1}^{N}(\chi_k/\tau_{v,k})$ at different streamwise locations. Starting from the plane B, the $\tau_{v,mix}$ in the inner core of the jet decreases to the order of 1 μs. In consideration that the flow residence timescale elongates due to flow deceleration by combustion heat release, therefore the full relaxation of energy occurs between the vibrational and translational-rotational modes. This explains why the mixture in the inner core of the fuel jet tends to thermal equilibrium state as displayed in Fig. 10. The $\tau_{v,mix}$ in the supersonic mainstream is more than 10^3 μs, such that the vibrational energy relaxation of the mixture is much slower, which renders a low T_v compared to T_{tr} there.

To further reveal the unsteady supersonic combustion, the time evolution of T_{tr} and T_v on the combustor central plane for case A was shown in Fig. 12, where $t_0 = 0.0024$s and $\Delta t = 10^{-5}$s. In Fig. 12 (a)–(c), because of the spatial non-uniformity in local equivalence ratio, it can be observed that the resulting combustible fluid packets near the shear layer are not continuous and the area and shape of the packets are changing along the flow direction, which will lead to combustion oscillations [43]. Further downstream, the discontinuous packets are combined to form a long high-temperature zone due to enhanced flow instability as displayed in Fig. 12 (d).

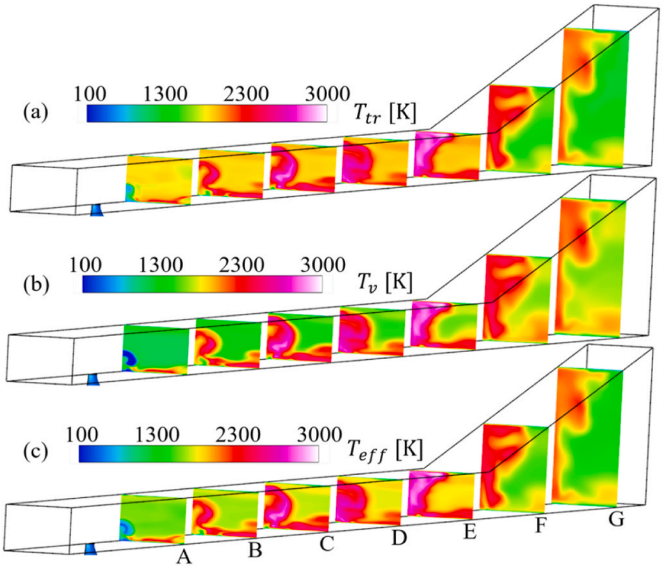

Fig. 10. Instantaneous contour of the (a) T_{tr}, (b) T_v and (c) T_{eff} at different streamwise locations.

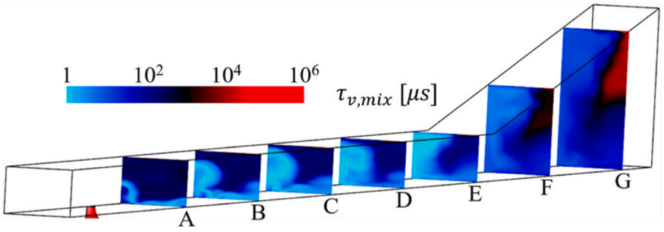

Fig. 11. Contours of vibrational relaxation timescale of the mixture ($\tau_{v,mix}$) at different streamwise locations.

In Fig. 12 (a)–(e), it can also be observed that the rise in vibrational temperature depends on the average translational-rotational temperature and area of the upstream packets. When the upstream packets are higher in translational-rotational temperature and larger in area, the vibrational temperature rises faster along the flow direction, implying a faster rate of energy exchange between different energy modes. This reflects the close coupling between turbulent combustion and thermal nonequilibrium effects in high Mach number supersonic combustion.

4.3. Flame dynamics under different thermal nonequilibrium conditions

In this section, influence of the thermal nonequilibrium condition on the flame dynamics will be illustrated. We first note that, though the total enthalpy is identical for both cases A and B at the combustor inlet, case B possesses a higher T_v compared to case A. In Fig. 13 (a), the T_{tr} distributions of the two cases are similar behind the bow shock, whereas the T_{tr} of case A is slightly higher in the vicinity of reflected shock waves because of the higher T_{tr} at the combustor inlet. As the mainstream is in vibrational heating state initially, low T_v will make T_{tr} decrease due to energy transfer. The weakened exothermic reaction subsequently reduces the rate of increase in the T_{tr} [14]. Thus, for case A with lower T_v, the high-temperature region on the jet windward side moves downstream considerably, and the high-temperature spans narrower in the transverse direction. With this physical process recognized, it is natural that the maximum value of T_{tr} for case B is higher near the shear layer where the chemical reactions are intensive. For $T_{tr} < 800$ K, the energy transfer between translational-rotational mode and vibrational mode is insignificant [15]. In this regard, in Fig. 13 (b), the increase of the T_v of the fuel jet downstream of the injector is mainly caused by the fuel-air mixing rather than energy transfer between molecules. For case B with higher T_v in the mainstream, the T_v of the fuel jet rises faster and the thermal equilibrium state is established more quickly. Eq. (24) illustrates the form of the T_{eff}, which is proportional to both T_{tr} and T_v. Before the position at $x \approx 0.08$ m, the T_{tr} distributions for both cases are similar, while the T_v for case B is obviously higher. Hence, as seen from Fig. 13 (c), the T_{eff} for case B is notably higher in the region after the bow shock and before the windward side of the fuel jet, which enhances local dissociation reactions.

As expected, for case B with higher T_v, more H and O radicals are formed near the shear layer because of the enhanced dissociation reactions, which can be seen in Fig. 14 (a) and (b). In addition to the faster reaction rate, the concentration peak values of H and O radicals are also higher in case B. These free atoms participate in the subsequent chain carrying reactions to generate other combustion products such as OH radicals in Fig. 14 (c). The OH radicals for both cases are formed in the vicinity of the fuel injector, exhibiting an early initiation of reactions. For case A with lower T_v, the location where the concentration of OH radicals distinctly increases is around $x = 0.120$ m, while for case B with higher T_v, x approaches 0.103 m. With the OH radical distribution delineating the location of the flame front, it is clear that higher T_v in Case B shortens the ignition delay time and allows the flame stabilization zone to move upstream. The jet-to-crossflow momentum flux ratio is, by definition, inversely proportional to the mainstream speed, which

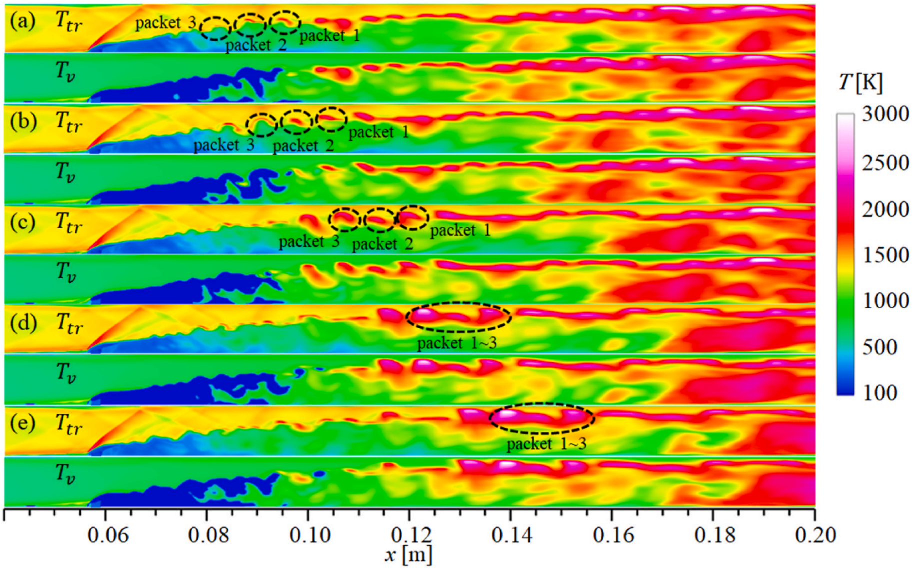

Fig. 12. Time evolution of T_{tr} and T_v for (a) $t = t_0$, (b) $t = t_0 + \Delta t$, (c) $t = t_0 + 2\Delta t$, (d) $t = t_0 + 3\Delta t$ and (e) $t = t_0 + 4\Delta t$ on the combustor central plane.

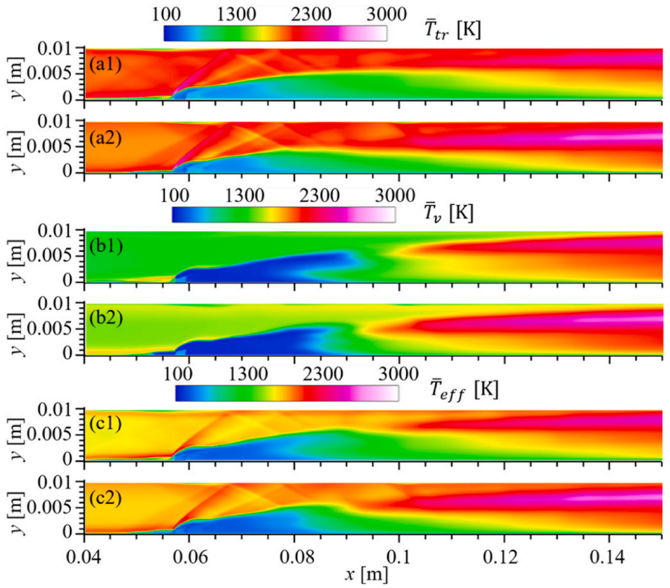

Fig. 13. Time-averaged (a) T_{tr}, (b) T_v, and (c) T_{eff} on the combustor central plane for both case A (top) and B (bottom), respectively.

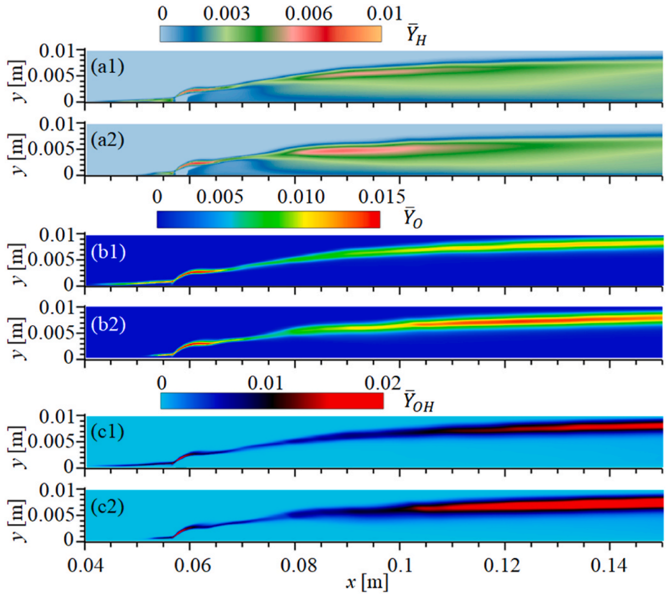

Fig. 14. Time-averaged mass fractions of (a) H radical, (b) O radical and (c) OH radical on the combustor central plane for both case A (top) and B (bottom), respectively.

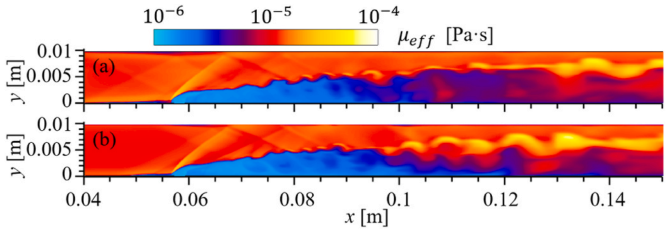

Fig. 15. Instantaneous contours of effective viscosity coefficient on the combustor central plane for both case A (top) and B (bottom), respectively.

is lower in case A. Thus, the penetration depth for case A is higher, which benefits the fuel-air mixing. We also note that due to the block effect of the fuel injection, the supersonic mainstream undergoes remarkable deceleration upstream the injection location where the local Mach is approximately between 0.3 and 1.2. This deceleration is accompanied by direct raise in translational-rotational temperature while the energy transfers to vibrational energy need longer relaxation time. Correspondingly, this leads to higher local Park's effective temperature for case A than for case B in the recirculation zone as can be seen in Fig. 13 (c). Thus with higher local overall temperature and combustion efficiency, the boundary layer flow bears higher heating load and has lower average density which makes it more likely to separate. Consequently, as can be seen in Fig. 14, an earlier separation of the wall boundary layer upstream the fuel injector occurs in case A.

The effective viscosity coefficients μ_{eff} on the combustor central plane for both cases are displayed in Fig. 15. From the combustor inlet to $x = 0.09$ m, there is not much dissimilarity in μ_{eff} between two cases. Theoretically, the viscosity increases as the T_{tr} increases. In Fig. 15, since the T_{tr} of the H_2 is only 300 K, the viscosity coefficients of the H_2 near the fuel injection are much lower than that of the mainstream. Further downstream, the heat released by the exothermic reactions increases T_{tr}, which consequently increases the local viscosity. For case B with higher T_v, the viscosity increases more sharply with the enhanced reactivity, which weakens the fuel-air mixing as the local Reynolds number increases.

Figs. 16–18 present the quasi one-dimensional (1D) combustion performance analyses, which are obtained by mass-weighted integration on cross sections at various streamwise locations. In Fig. 16 (a), downstream the fuel injector, although considerable discrepancy can be found in T_{tr} on the combustor central plane, the quasi-1D T_{tr} for the two cases almost overlap. In contrast, both in the combustor section and the exhaust nozzle, the T_v of case B is always higher than case A, which enhances the reactivity. Regarding the form of the energy exchange source term in Eq. (16), it can be seen that the energy exchange source term is proportional to the disparity between e_{tr} and e_v. As such, for case A with lower T_v, the T_v increases more rapidly after entering the combustor. Nevertheless, the temperature difference $|T_v - T_{tr}|$ of case B is smaller in the combustor section, which means that the flow field in case B is closer to the thermal equilibrium state overall. At the downstream locations, in the exhaust nozzle, as translational-rotational energy is partially converted into kinetic energy, T_{tr} drops rapidly and the flow field deviates from the thermal equilibrium state again, which is consistent with the findings in Section 4.2.

From Fig. 16 (b), the recirculation zone upstream the fuel injection causes a decline in local Mach number. For case A, the position where Mach number begins to decline is closer to the combustor inlet due to wall boundary layer. Quantitatively, as more heat is released by the reaction downstream, the deceleration from the inlet to the combustor outlet in case B is 34.72%, which is larger than 28.58% in case A. For this reason, the flow residence time in case B is relatively longer, which facilitates the exchange of energy amongst different modes.

In Fig. 17 (a), the mixing efficiencies for both cases in the combustor section are monotonically increasing downstream of the fuel injector location. In case B, higher T_v, lower penetration height and higher local viscosity all inhibit the mixing between the fuel and airstream, thereby leading to lower mixing efficiency of case B compared to case A after fuel injection. Nevertheless, the final mixing efficiencies at the end of the combustion section achieve approximately 100% in both cases.

The combustion reaction rates at high Mach number conditions are limited by the fuel-air mixing, which is typical of the mixing-controlled combustion scenarios. Correspondingly, the combustion efficiencies also tend to increase monotonically after the fuel injection as shown in Fig. 17 (b). Even with enhanced reactivity, for case B with higher T_v, the combustion efficiency in the combustor section has been more affected by the mixing, which is slightly lower than that in case A. For case B, the combustion efficiency still increases in the exhaust nozzle under enhanced reactivity, while it almost peaks at the end of the combustor section for case A. The final combustion efficiencies are 76% and 84% for case A and case B, respectively. It was concluded that increasing T_v at the inlet is beneficial to obtain better combustion performance.

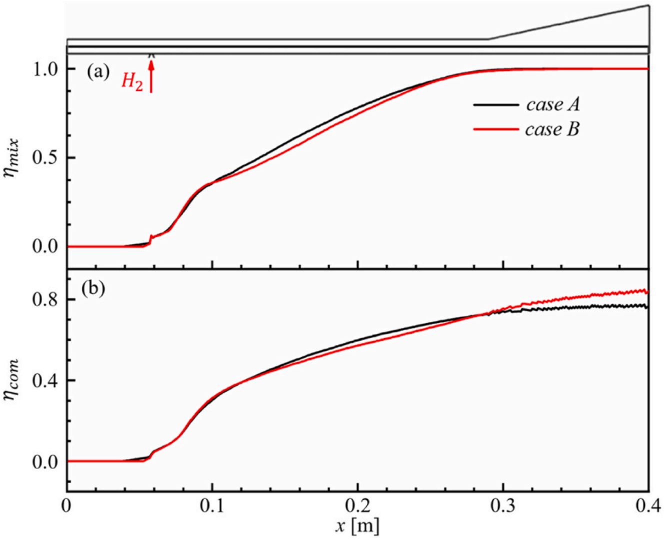

Fig. 17. Quasi one-dimensional distribution along the streamwise direction for time-averaged (a) mixing efficiency and (b) combustion efficiency for case A and B, respectively.

In Fig. 18 (a), a local peak value of $d\dot{Q}$ distribution can be observed upstream of the fuel injector, which is due to the presence of the low-speed recirculation zone where the fuel reacts with air and releases a small amount of heat. As the combustion reactions occur consistently in the combustor section, the $d\dot{Q}$ maintains a high level. There are discrepancies in the heat release between the two cases, but the quasi-1D distribution of T_{tr} for the two cases are very close, which is owing to the close T_{tr} of their mainstreams initially. The $d\dot{Q}$ decreases sharply in the exhaust nozzle, which is attributed to the reduction in the chemical reaction rates under remarkably decreased T_{tr} and T_v. After $x = 0.25$ m,

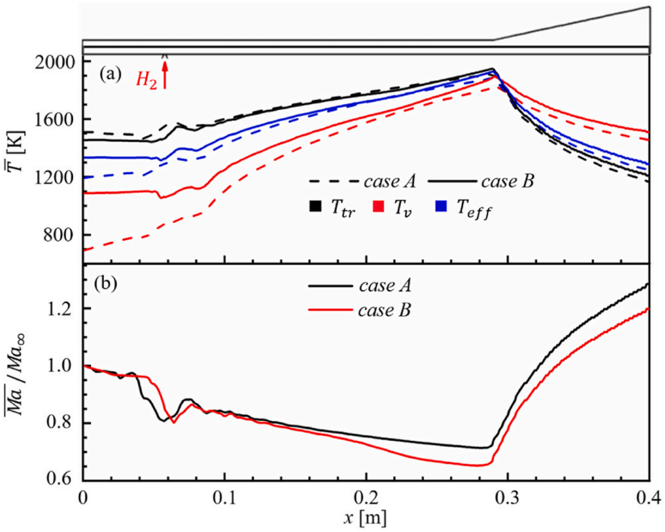

Fig. 16. Quasi one-dimensional distribution along the streamwise direction for time-averaged (a) temperature and (b) Mach number for case A and B, respectively.

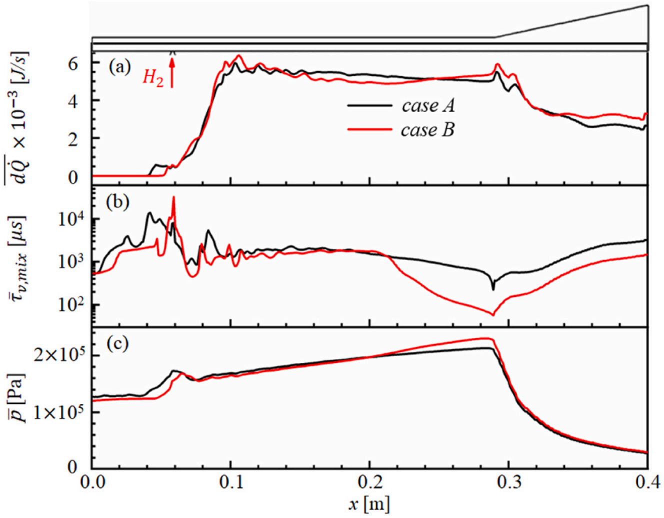

Fig. 18. Quasi one-dimensional distribution along the streamwise direction for time-averaged (a) heat release rate, (b) vibrational relaxation timescale of the mixture, and (c) static pressure for case A and B, respectively.

the mixing efficiencies of the two cases are similar, but more heat is released in case B due to faster chemical reactions, which is consistent with the results in Fig. 17 (b).

Since the change in temperature is the main trigger for the thermal nonequilibrium, it is more likely to occur in the shocks, expansion waves and reaction zone where the temperature changes drastically. The combustor inlet retains the reflected shocks generated in the inlet ramp, while the shock structures in the vicinity of the fuel injection are complex. Consequently, in Fig. 18 (b), the $\tau_{v,mix}$ increases significantly after entering the combustor and shows a strong oscillation near the fuel injection. The $\tau_{v,mix}$ is approximately 10^3 μs downstream of the fuel injection, and the energy transfer among various modes is quite slow. While the vibrational relaxation timescale is comparable to the flow characteristic timescale there, the thermal nonequilibrium effect and turbulent combustion will be closely coupled. As seen in Eq. (18), $\tau_{v,mix}$ is inversely proportional to T_{tr} and static pressure. As it was known from section 4.2 that the flow field has not yet reached the turbulent combustion stage until $x = 0.2$ m. Thus, the high temperature region of the T_{tr} is still only distributed in the vicinity of the shear layer, while the T_{tr} in the external air mainstream is still low. Since the $\tau_{v,mix}$ is inversely proportional to the T_{tr}, the $\tau_{v,mix}$ only starts to decrease significantly after $x = 0.2$ m. Additionally, it can also be seen from Fig. 18 (c) that the rise of static pressure in case B is faster after $x = 0.2$ m due to the higher overall combustion efficiency. The $\tau_{v,mix}$ is inversely proportional to the static pressure such that the $\tau_{v,mix}$ of case B decreases more sharply after $x = 0.2$ m as can be seen in Fig. 18 (b). Correspondingly, for case B, the $\tau_{v,mix}$ decreases to 56.49 μs at the end of the combustor section, which is much lower than that for case A (220.03 μs). It is clear that the higher T_v at the combustor inlet promotes the restoration of the thermal equilibrium state.

To better understand the coupling between the thermal nonequilibrium and chemical reactions, Figs. 19 and 20 present realizations of (T_{tr}, T_v) at cut plane B, C, E and G, colored by mixture fraction Z and Mach number, respectively. In Figs. 19 and 20, the values for both T_{tr} and T_v range from 100 to 2700 K. At plane B, the shape of the difference $T_{tr}- T_v$ distribution resembles an obtuse triangle. In Fig. 19 (a1), the mixture fractions of the long side and short sides represent to the maximum and minimum values, respectively. The long side of the obtuse triangle corresponds to the fuel jet side, while the two short sides correspond to the mainstream. From Fig. 19 (b1) and (b2), it can be found that the mixture fraction is slightly higher in case B, which confirms that case A is more sufficiently mixed than case B in the combustor section.

In Fig. 20 (a1), Mach number of the lower short side is smaller, which corresponds to the mainstream closer to the combustor bottom wall. Also in Fig. 19 (a1) and (a2), the mainstream is in vibrational heating state initially, while the fuel jet is in vibrational cooling state because part of the translational-rotational energy is transferred to kinetic energy when the fuel is injected. As the combustion releases heat, both T_{tr} and T_v increase obviously along the streamwise direction, and the maximum temperature rises to nearly 2500 K. In addition, Mach number of the mainstream decreases gradually. With the exchange of translational-rotational and vibrational energy, T_v approaches T_{tr} and thermal equilibrium state is established gradually, which shown in Fig. 20 (c1) and (c2). With shorter relaxation time and longer residence time, the vibrational energy in case B increases more rapidly. Therefore, it is clear that $T_{tr} - T_v$ distribution of case B is much closer to the line of $T_{tr} = T_v$ overall, meaning a larger region of thermal equilibrium state. In Fig. 20 (d1) and (d2), after entering the exhaust nozzle, T_v is higher than T_{tr} almost everywhere, which represents the vibrational cooling state.

Respectively, Figs. 21 and 22 display the frequency spectrum of the pressure and the heat release rate fluctuation sampled at locations SP1 to SP4 with a fixed time interval of $\Delta t = 1.5 \times 10^{-9}$ s, which are located in the jet shear layer as denoted in Fig. 8. Additionally, the strong shock-combustion interactions cause considerable instabilities to the supersonic combustion [43–45]. In Fig. 21 (a), for case A and case B, the dominant frequencies with a large amplitude are 2.95×10^5 Hz and 2.67×10^5 Hz at SP1 respectively, which is related to the R-M instability caused by the reflected shock waves as shown in Fig. 8. The higher amplitudes of the pressure fluctuation are observed in case B. This is also consistent with previous studies [46,47], in which the longer and higher mixing area in the combustor is susceptible to pressure oscillations due to the insufficient and unevenly distributed local equivalence ratios. From Fig. 21 (b)–(d), the amplitudes of pressure fluctuation decline significantly as a result of the attenuation of the shock waves' strength. The pressure oscillation in the mixing and auto-ignition zone diminishes substantially. It can also be found that in Fig. 22 (a), the amplitudes are large in the frequency range of $10^5 - 10^6$ Hz, which is caused by the existence of eddies with various time scales. The oscillation of the heat release rate decreases gradually at downstream location, but the amplitude of heat release rate fluctuation at SP2 are not negligible which indicates that the oscillation at this location is related to combustion instability. The amplitudes of heat release rate fluctuation of case B are markedly larger. These finding suggests that increasing the T_v of combustor inlet leads to more unstable ignition process by enhanced reactivity.

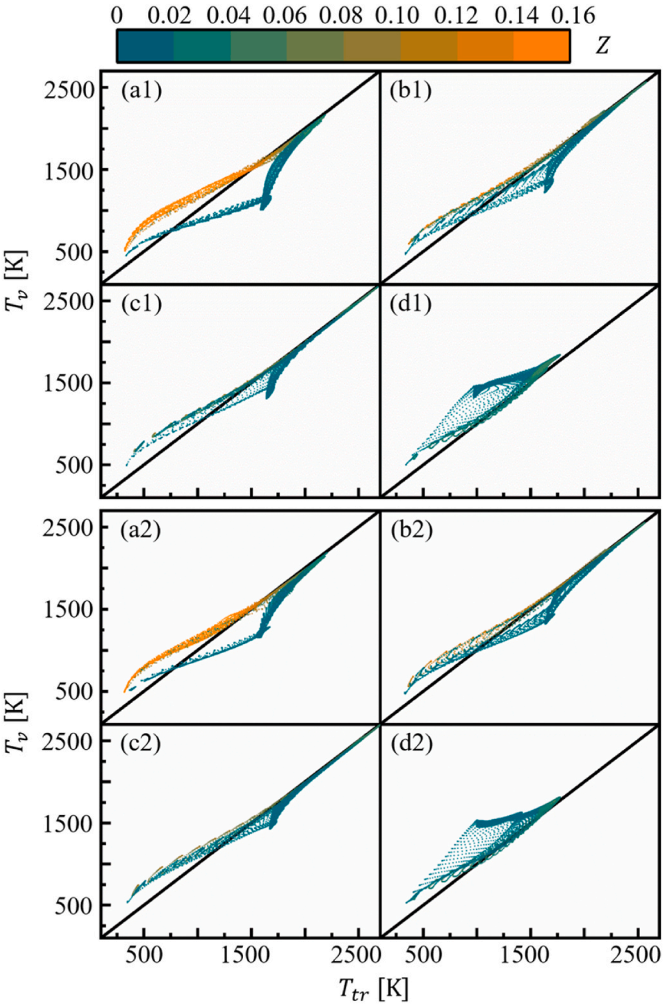

Fig. 19. Realizations of T_{tr} and T_v on the planes B, C, E and G respectively colored by mixture fraction for case A (a1-d1) and B (a2-d2).

5. Concluding remarks

This study focused on the combustion dynamics of HyShot II scramjet engine under different combustor inflow thermal nonequilibrium conditions. For the nonequilibrium combustion simulations, the two-

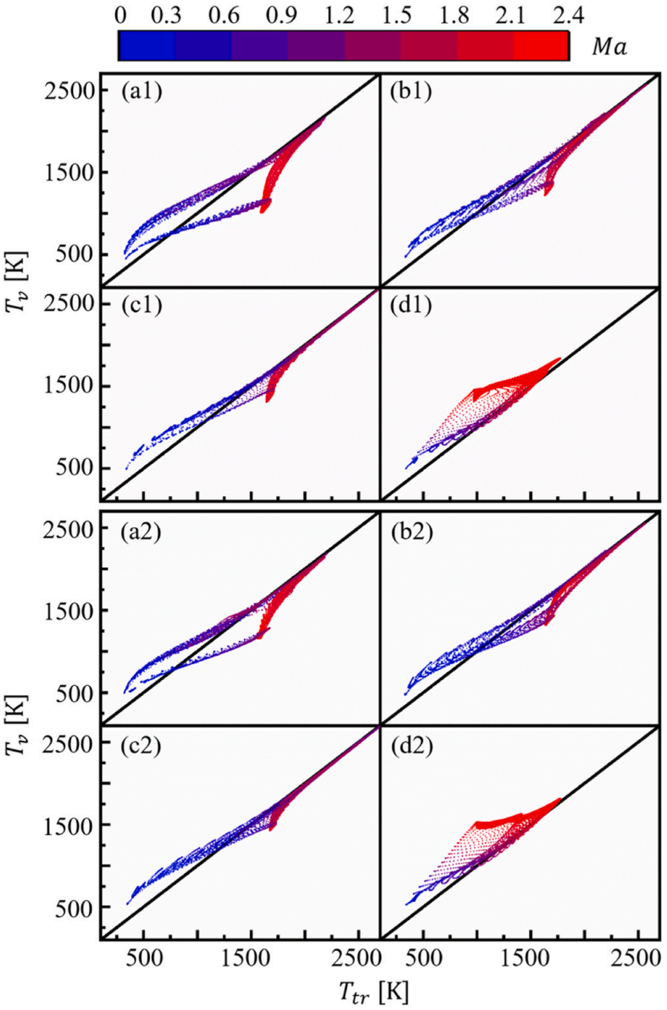

Fig. 20. Realizations of T_{tr} and T_v on the planes B, C, E and G respectively colored by Mach number for case A (a1-d1) and B (a2-d2).

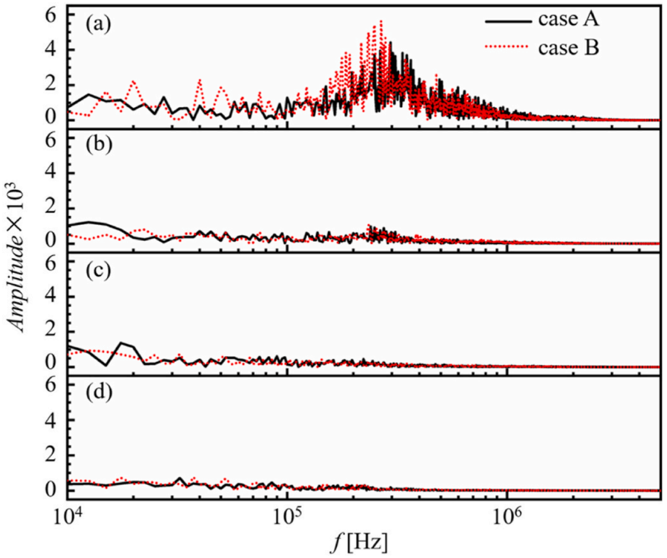

Fig. 21. Spectrum of the pressure fluctuation sampled at locations (a) SP1, (b) SP2, (c) SP3, and (d) SP4, respectively.

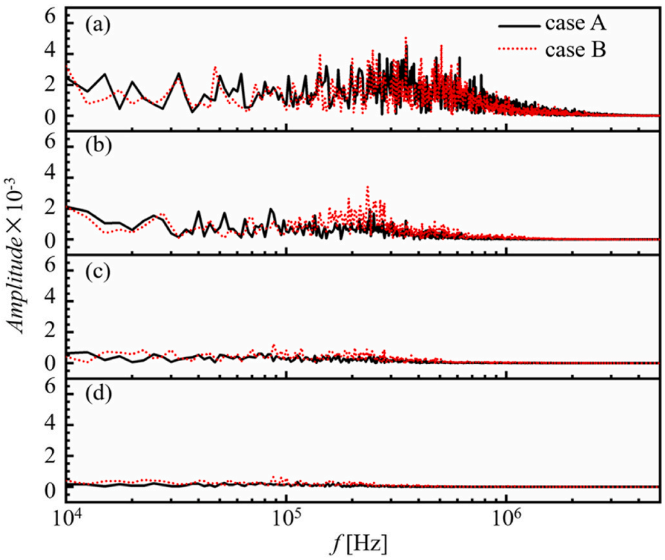

Fig. 22. Spectrum of the heat release rate fluctuation sampled at locations (a) SP1, (b) SP2, (c) SP3, and (d) SP4, respectively.

temperature framework of Park was employed with the Landau-Teller relaxation model and Millikan-White thermal relaxation coefficients. The vibration-chemistry coupling was handled with the Park T-Tv model in combination with a 7-species and 9-reactions chemical mechanism for hydrogen oxidation. The simulation results compared favorably with the ground-based experiment measurements. Two typical cases with the same total enthalpy whereas differ in vibrational temperature were comparatively studied concerning the flame structure, mixing and combustion efficiency as well as the dynamical characteristics. The main concluding remarks of the present work are as follow.

With thermal nonequilibrium inflow condition, there will be a noticeable stratification in the thermal state in the circumferential direction both in the combustor section and exhaust nozzle. In the inner core where the fuel mixes with the mainstream, flow deceleration caused by the heat release leads to a sufficient transformation of energy between the vibrational and translational-rotational modes, and the thermal equilibrium state is established quickly. However, the $\tau_{v,mix}$ is larger than 10^3 μs in the supersonic mainstream, where the thermal nonequilibrium dominates.

For inflow under higher T_v, the fuel jet's penetration height is lower while the local viscosity is higher which hinders the mixing between the fuel and air stream. However, a 400 K increase in inflow T_v results in a higher effective temperature, which promotes the dissociation reaction rates and thus shortens the ignition distance. The corresponding combustion efficiency for case A ($T_v = 688.38$ K) and B ($T_v = 1088.42$ K) are 76% and 84%. With better combustion performance, there is an additional 6% deceleration in the supersonic mainstream and the energy exchange rate between vibrational and translational-rotational modes is almost four times faster at the combustor outlet, which facilitates the restoration of thermal equilibrium. Furthermore, under higher inflow vibrational temperature, the jet flame in supersonic crossflow becomes more unstable with noticeable fluctuations in combustion heat release and local static pressure.

Declaration of competing interest

The authors declare that they have no known competing financial interests or personal relationships that could have appeared to influence the work reported in this paper.

Acknowledgement

This work was supported by the National Key Project (Grant No. GJXM92579), the Strategic Priority Research Program of Chinese Academy of Sciences (Grant No. XDA17030100) and the High-level Innovation Research Institute Program of Guangdong Province (Grant No. 2020B0909010003).

Appendix A

To ensure the shock capturing capacity of the present solver, it was further validated against the Lehr's shock-induced combustion experiment. The experiment [48] was performed on a semi-sphere with a cylinder whose radius was 7.5 mm and the height of the cylinder was 15 mm. As shown in Fig. 23, half of the experimental model was considered for this simulation due to geometric symmetry, with a total grid cells number of 1.26 million. Grid refinements were imposed to the vicinity of the walls and the shock front. The chemical reaction mechanism is the same as that used in the combustor simulation as detailed in section 2.2. The walls are treated as non-catalytic, non-slip and adiabatic condition. The temporal integration was advanced by the first-order Euler scheme. The integration was constrained by a maximum Courant-Friedrichs-Lewy number of 0.1, corresponding to an approximate average time step of 8×10^{-10}s. The Mach number of the mainstream is 6.46, and other operating conditions are given in Table 7. We also noted that since the mainstream Mach number is 6.46, the solver was operating in single temperature formulation, wherein the validation was focused on the shock-combustion interaction.

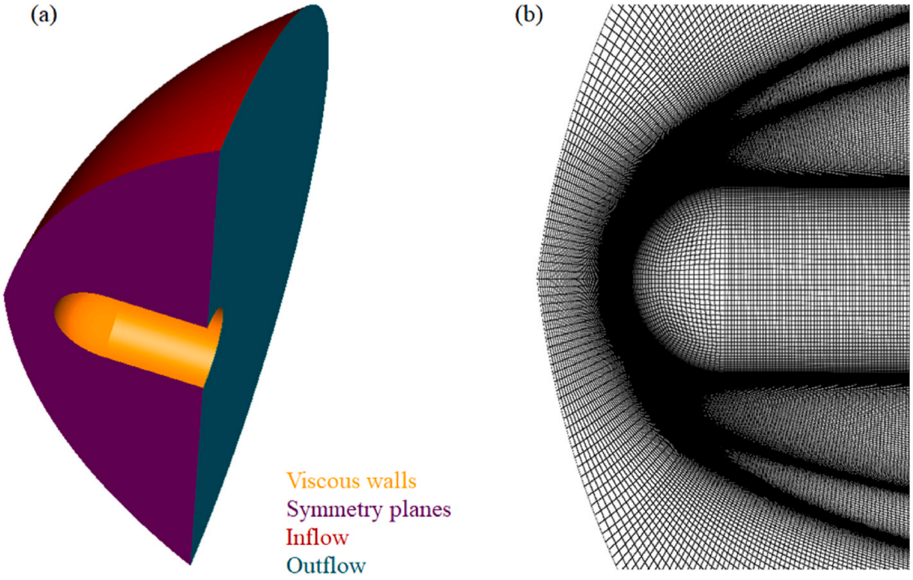

Fig. 23. Schematic of (a) the simulation model and (b) the computational mesh.

Table 7
Mainstream inflow conditions of shock-induced super-detonative combustion [48].

Property	Ma_∞	p_∞ [kPa]	T_∞ [K]	Mass fraction of species		
				$Y_{H_2,\infty}$	$Y_{O_2,\infty}$	$Y_{N_2,\infty}$
Value	6.46	42.663	293	0.0285	0.2264	0.7451

In Fig. 24 (a), the density gradient of the simulation is compared with the Schlieren image of the experiment [48], and the result shows that the present simulation well reproduced the shock stand-off distance. In addition, both the bow shock position and combustion front show excellent consistency with experimental measurement as shown in Fig. 24 (b). It can also be found in Fig. 25 that good agreement of pressure, temperature and density distribution along the stagnation line between the reference data [49] and the present simulation results are achieved, which confirms the reliability of the present solver.

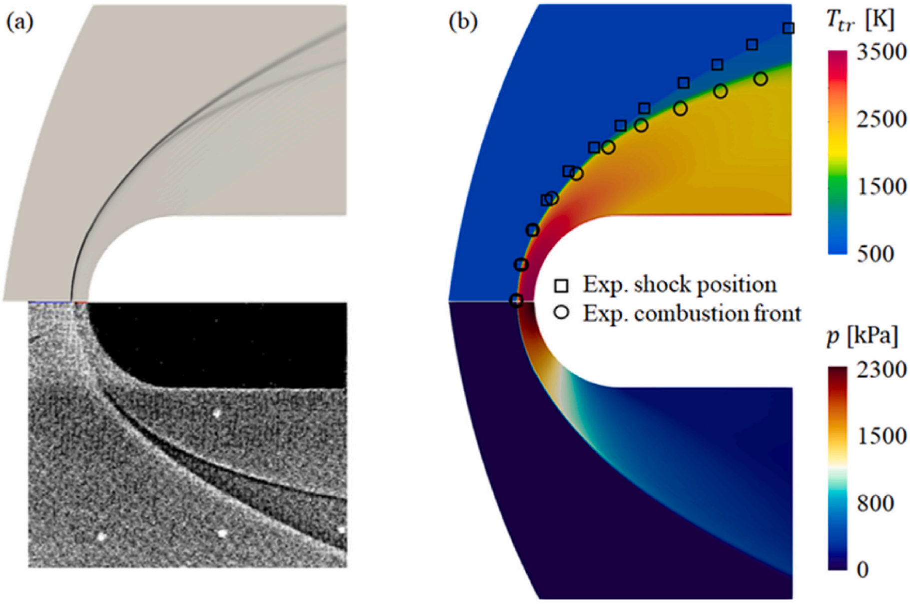

Fig. 24. Time-averaged (a) density gradient distribution compared with the Schlieren image [48] and (b) temperature and pressure distribution on the symmetry plane.

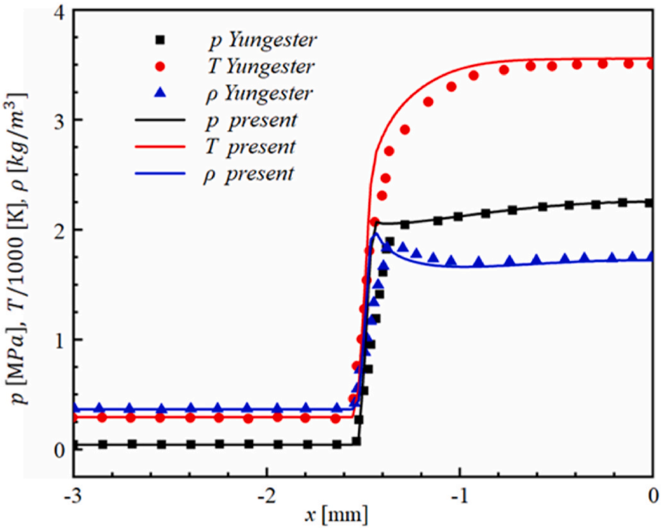

Fig. 25. Comparison of Yungester's reference data [49] and present simulation results along the stagnation line.

References

[1] N. Das, K.M. Pandey, K.K. Sharma, A brief review on the recent advancement in the field of jet engine - scramjet engine, Mater. Today: Proc. 45 (2021) 6857–6863.
[2] R.N. Gupta, J.M. Yos, R.A. Thompson, et al., A Review of Reaction Rates and Thermodynamics and Transport Properties for the 11-Species Air Model for Chemical and Thermal Nonequilibrium Calculations to 30000K, NASA Report 1232, NASA Langley Research Center, Washington, U.S.A, 1990.
[3] R.M. Gehre, V. Wheatley, R.R. Boyce, Computational investigation of thermal nonequilibrium effects in scramjet geometries, J. Propul. Power 29 (2013) 648–660.
[4] D. Vatansever, B. Celik, An open-source hypersonic solver for non-equilibrium flows, J. Aeronaut. Sp. Technol. 14 (2021) 35–52.
[5] V. Casseau, D.E.R. Espinoza, T. Scanlon, et al., A two-temperature open-source CFD model for hypersonic reacting flows, part two: multi-dimensional analysis, Aerospace 3 (2016) 45.
[6] Y. Du, S. Sun, M. Tan, et al., Non-equilibrium simulation of energy relaxation for earth reentry utilizing a collisional-radiative model, Acta Astronaut. 193 (2022) 521–537.
[7] F. Zuo, S. Hu, Thermochemical non-equilibrium effects on aerothermodynamic prediction of laminar double-cone flow, Acta Astronaut. 182 (2021) 179–188.
[8] I. Nompelis, G.V. Candler, M.S. Holden, Effect of vibrational nonequilibrium on hypersonic double-cone experiments, AIAA J. 41 (2003) 2162–2169.
[9] S. Han, B.J. Lee, B.J. Lee, Numerical analysis of thermochemical nonequilibrium flows in a model scramjet engine, Energies 13 (2020) 606.
[10] R. Fiévet, V. Raman, Effect of vibrational nonequilibrium on isolator shock structure, J. Propul. Power 34 (2018) 1334–1344.
[11] S. Voelkel, V. Raman, P.L. Varghese, Effect of thermal nonequilibrium on reactions in hydrogen combustion, Shock Waves 26 (2016) 539–549.
[12] C. Park, Assessment of two-temperature kinetic model for ionizing air, J. Thermophys. Heat Tran. 3 (1989) 233–244.
[13] R. Fiévet, S. Voelkel, H. Koo, et al., Effect of thermal nonequilibrium on ignition in scramjet combustors, Proc. Combust. Inst. 36 (2017) 2901–2910.
[14] H. Koo, V. Raman, P.L. Varghese, Direct numerical simulation of supersonic combustion with thermal nonequilibrium, Proc. Combust. Inst. 35 (2015) 2145–2153.
[15] W. Yao, Nonequilibrium effects in hypersonic combustion modeling, J. Propul. Power 38 (2022) 1–17.
[16] S.-H. Won, I.-S. Jeung, J.-Y. Choi, Numerical analysis of dynamic combustion in HyShot scramjet combustor with a transverse fuel injection, J. Korean Soc. Combust. 12 (2007) 1–9.
[17] H.G. Hornung, Ground Testing for Hypervelocity Flow, Capabilities and Limitations, California Institute of Technology, Pasadena, California, U.S.A, 2010.

[18] M.L. Shur, P.R. Spalart, M.K. Strelets, et al., A hybrid RANS-LES approach with delayed-DES and wall-modelled LES capabilities, Int. J. Heat Fluid Flow 29 (2008) 1638–1649.

[19] K. Hannemann, S. Karl, J.M. Schramm, et al., Methodology of a combined ground based testing and numerical modelling analysis of supersonic combustion flow paths, Shock Waves 20 (2010) 353–366.

[20] R. Fiévet, Impact of Vibrational Nonequilibrium on the Simulation and Modeling of Dual-Mode Scramjets, The University of Michigan, Ann Arbor, Michigan, U.S.A, 2018.

[21] J.D. Anderson, Hypersonic and High Temperature Gas Dynamics, second ed., American Institute of Aeronautics and Astronautics, Reston, Virginia, U.S.A, 2006.

[22] R.D.J. III, NIST Computational Chemistry Comparison and Benchmark Database, NIST Standard Reference Database Number 101, Release 18, October 2016. http://cccbdb.nist.gov/.

[23] M.J. Wright, D. Bose, G.E. Palmer, et al., Recommended collision integrals for transport property computations part 1: air species, AIAA J. 43 (2005) 2558–2564.

[24] S. Gordon, B.J. McBride, F.J. Zeleznik, Computer Program for Calculation of Complex Chemical Equilbrium Compositions and Applications Supplemnet I-Transport Properties, NASA Lewis Research Center, Cleveland, Ohio, 1984. U.S.A.

[25] P. Spalart, S. Allmaras, A one-equation turbulence model for aerodynamic flows, in: 30th Aerospace Sciences Meeting and Exhibit, 1992. Reno, NV, U.S.A.

[26] K. Wu, P. Zhang, X. Fan, On jet-wake flame stabilization in scramjet: a LES/RANS study from chemical kinetic and fluid-dynamical perspectives, Aero. Sci. Technol. 120 (2022), 107255.

[27] L. Landau, E. Teller, On the theory of sound dispersion, Coll. Pap. L.D. Landau. 10 (1965).

[28] R.C. Millikan, D.R. White, Systematics of vibrational relaxation, J. Chem. Phys. 39 (1963) 3209–3213.

[29] C. Park, Nonequilibrium Hypersonic Aerothermodynamics, Wiley International, New York, NY, U.S.A, 1990.

[30] A. Zidane, R. Haoui, M. Sellam, et al., Numerical study of a nonequilibrium H2−O2 rocket nozzle flow, Int. J. Hydrogen Energy 44 (2019) 4361–4373.

[31] V. Casseau, R.C. Palharini, T.J. Scanlon, et al., A two-temperature open-source CFD model for hypersonic reacting flows, part one: zero-dimensional analysis, Aerospace 3 (2016) 34.

[32] Y. Zheng, C. Yan, Y. Zhao, Uncertainty and sensitivity analysis of inflow parameters for HyShot II scramjet numerical simulaiton, Acta Astronaut. 170 (2020) 342–353.

[33] S. Karl, K. Hannemann, CFD analysis of the HyShot supersonic combustion flight experiment configuration, in: 14th AIAA/AHI Space Planes and Hypersonic Systems and Technologies Conference, 2006. Canberra, Australia.

[34] M. Chapuis, E. Fedina, C. Fureby, et al., A computational study of the HyShot II combustor performance, Proc. Combust. Inst. 34 (2013) 2101–2109.

[35] W. Yao, K. Wu, X. Fan, Influences of domain symmetry on supersonic combustion modeling, J. Propul. Power 35 (2019) 451–465.

[36] Y. Zhao, H. Huang, Numerical study of hypersonic surface heat flux with different air species models, Acta Astronaut. 169 (2020) 84–93.

[37] S. Karl, K. Hannemann, A. Mack, et al., CFD analysis of the HyShot II scramjet experiments in the HEG shock tunnel, in: 15th AIAA International Space Planes and Hypersonic Systems and Technologies Conference, Dayton, Ohio, U.S.A, 2008.

[38] S. Chen, D. Zhao, RANS investigation of the effect of pulsed fuel injection on scramjet HyShot II engine, Aero. Sci. Technol. 84 (2019) 182–192.

[39] A. Kurganov, E. Tadmor, New high-resolution central schemes for nonlinear conservation laws and convection–diffusion equations, J. Comput. Phys. 160 (2000) 241–282.

[40] A. Ben-Yakar, R.K. Hanson, Experimental investigation of flame-holding capability of hydrogen transverse jet in supersonic cross-flow, Symp. (Int.) Combust. 27 (1998) 2173–2180.

[41] A.F. Moura, V. Wheatley, I. Jahn, Thermofluidic compression effects to achieve combustion in a low-compression scramjet engine, Shock Waves 28 (2017) 863–875.

[42] M. Sun, H. Wang, Z. Cai, et al., Unsteady Supersonic Combustion, Springer, 2020.

[43] H. Wang, Z. Wang, M. Sun, et al., Large-Eddy/Reynolds-averaged Navier–Stokes simulation of combustion oscillations in a cavity-based supersonic combustor, Int. J. Hydrogen Energy 38 (2013) 5918–5927.

[44] R. Feng, Y. Huang, J. Zhu, et al., Ignition and combustion enhancement in a cavity-based supersonic combustor by a multi-channel gliding arc plasma, Exp. Therm. Fluid Sci. 120 (2021).

[45] M.-B. Sun, Z. Zhong, J.-H. Liang, et al., Experimental investigation of supersonic model combustor with distributed injection of supercritical kerosene, J. Propul. Power 30 (2014) 1537–1542.

[46] Z. Cai, X. Zhu, M. Sun, et al., Experiments on flame stabilization in a scramjet combustor with a rear-wall-expansion cavity, Int. J. Hydrogen Energy 42 (2017) 26752–26761.

[47] Z. Cai, J. Zhu, M. Sun, et al., Ignition processes and modes excited by laser-induced plasma in a cavity-based supersonic combustor, Appl. Energy 228 (2018) 1777–1782.

[48] H.F. Lehr, Experiments on shock-induced combustion, Acta Astronaut. 17 (1972) 589–597.

[49] S. Yungster, S. Eberhardt, A.P. Bruckner, Numerical simulation of hypervelocity projectiles in detonable gases, AIAA J. 29 (1991) 187–199.